

Discovery of Polar Semiconducting Scandium Nitride as an Infrared Plasmon and Phonon-Polaritonic Material

Krishna Maurya

Jawaharlal Nehru Centre for Advanced Scientific Research

Dheemahi Rao

Jawaharlal Nehru Centre for Advanced Scientific Research

Shashidhara Acharya

Jawaharlal Nehru Centre for Advanced Scientific Research

Pavithra Rao Rao

Indian Institute of Science

Ashalatha Pillai

The University of Sydney

Shankar Selvaraja

Indian Institute of Science

Magnus Garbrecht

The University of Sydney

Bivas Saha (✉ bsaha@jncasr.ac.in)

Jawaharlal Nehru Centre for Advanced Scientific Research <https://orcid.org/0000-0002-0837-1506>

Article

Keywords:

Posted Date: January 19th, 2022

DOI: <https://doi.org/10.21203/rs.3.rs-1267475/v1>

License:   This work is licensed under a Creative Commons Attribution 4.0 International License.

[Read Full License](#)

Abstract

Interaction of light with collective charge oscillations termed as plasmon-polariton and with polar lattice vibrations termed phonon-polariton is a new frontier in nano-photonics. Traditionally doped-semiconductors and conducting metal oxides (CMO) are used to achieve plasmon-polaritons in the near-to-mid infrared (IR), while polar dielectrics are utilized for realizing phonon-polaritons in the long-wavelength IR (LWIR) spectral regions. However, demonstrating plasmon- and phonon-polariton in one host material with low-loss is challenging due to the mutually conflicting physical property requirements. In this article, we demonstrate high-quality tunable short-wavelength IR (SWIR) plasmon-polariton and LWIR phonon-polariton in complementary metal-oxide-semiconductor (CMOS) compatible group III-V polar semiconducting scandium nitride (ScN) thin films. We achieve both resonances by utilizing *n*-type (oxygen) and *p*-type (magnesium) doping in ScN that allows modulation of carrier concentration from 5×10^{18} to $1.6 \times 10^{21} \text{ cm}^{-3}$. Our work enables infrared nano-photonics with an epitaxial group-III semiconducting nitride, opening the possibility for practical applications.

Full Text

Polaritons, the hybrid quasiparticles of photons and electric dipoles¹⁻³ (collective free electron oscillations, optical lattice vibrations or excitons) have attracted significant interest for numerous infrared nano-photonics applications⁴ including nano-laser^{5,6}, non-linear optics⁷⁻⁹, heat-harvesting¹⁰⁻¹² etc. Due to their sub-diffraction mode confinement and field enhancement, plasmon- and phonon-polaritons are also researched extensively for overcoming the fundamental resistance-capacitance (RC) delay in electronics and the diffraction limit in photonic devices^{13,14}. However, applications of polaritons in practical devices so far are limited primarily due to the significant optical losses arising from the scattering of the free electrons and optical phonon modes. Therefore, materials exhibiting low-loss and high-quality plasmon-polariton in the near-to-mid IR and phonon-polaritons in the LWIR are in great demand¹⁵. Practical applications also require that such materials should exhibit structural and high-temperature stability, CMOS compatibility, ease-of-fabrication, ease-of-integration with existing optoelectronic devices, and abundance.

Achieving plasmon resonance in the IR region of the electromagnetic spectrum requires materials to exhibit carrier concentration in the 10^{19} - 10^{21} cm^{-3} range with high carrier mobilities. Further, to accomplish low-losses, such materials should not exhibit interband/intraband transitions in the wavelength range of interest and should comprise a low defect density. As a result, heavily doped semiconductors such as *n*-type InAs¹⁶, *n*-type and *p*-type Si¹⁷, CMOs¹⁸ such as indium tin oxide (ITO), aluminum-doped zinc oxide (AZO), gallium-doped zinc (GZO) oxide, cadmium oxide (CdO)^{19,20}, patterned graphene structures^{21,22}, and semiconductor meta-surfaces²³ are used as plasmonic materials in the near (0.8-1.4 μm) and mid (3-15 μm)-IR spectral ranges. However, achieving low-loss high-quality plasmon resonance in the SWIR (1.4-3 μm) spectral region with high-mobility materials has been challenging. SWIR is an important spectral window for long-distance telecommunication (1.260-1.675

μm), hyperspectral imaging, solar cell, electronic board and produce inspection, anti-counterfeiting, surveillance, and a host of other applications^{14,24}.

Achieving phonon-polaritons, on the other hand, requires polar dielectric materials, where macroscopic electric field stiffens the force constant of the longitudinal-optical (LO) phonons and splits the LO and transverse-optical (TO) phonon modes at the zone center²⁵. Within the frequency range bounded by the LO and TO, termed as the *Reststrahlen* band, the real component of the dielectric permittivity (ϵ_1) becomes negative, and electromagnetic modes couple to the TO phonon giving rise to its evanescent character and confinement at the surface. Such confined surface-phonon-polariton (SPh.P) has emerged as a promising light-matter coupling mechanism in the LWIR range and several other applications such as passive radiative cooling, bio-molecular fingerprinting, diagnosis tools for cancer and dentistry detection are proposed^{24,26}. So far, excitation and engineering of SPh.P are performed with well-established dielectric materials such as 4H-SiC²⁷, h-BN²⁸, or AlN²⁹ with large bandgap and low carrier densities.

Due to the conflicting physical property requirements, demonstration of plasmon- and phonon-polaritons in one host material has been challenging. Conceptually, achieving plasmon and phonon-polariton in one host material is possible if the electronic and phonon resonances are spectrally separated from each other (see Eq. 1 for the total dielectric permittivity), and the carrier concentration can be tuned from as low as 10^{18} to 10^{21} cm^{-3} while retaining a moderately high mobility at the same time. To achieve this, dopants should not introduce defect states inside the bandgap of semiconductors that otherwise could pin the Fermi level. Additionally, dopant states should not alter the valence and/or conduction band edges, which could drastically change carrier effective mass and mobility. Satisfying all of the conditions has proven quite challenging for most well-established semiconductors.

$$\epsilon_{total}(\omega) = \epsilon \left(1 - \frac{\omega_p^2}{\omega^2 - i\gamma\omega} + \frac{\omega_{LO}^2 - \omega_{TO}^2}{\omega_{TO}^2 - \omega^2 - i\omega\Gamma} \right) \quad (1)$$

$$\omega_p = \sqrt{\frac{ne^2}{m^* \epsilon_0}}$$

2

$$\epsilon_{plasmon}(\omega) = - \frac{\omega_p^2}{\omega^2 - i\gamma\omega}$$

3

Where, $\epsilon_{total}(\omega)$ is the total dielectric permittivity²⁴ with contributions from the plasmon or Drude component (second term) and phonon (third term) resonances. ϵ_0 , ω_p , ω_{LO} , ω_{TO} , γ , Γ , n and m^* are the high-frequency dielectric constant, plasma frequency, longitudinal optical and transverse optical phonon frequencies, plasmon and phonon damping constants, carrier concentration and effective mass respectively.

In this work, we demonstrate that *n*-type (oxygen) and *p*-type (magnesium)-doping in epitaxial ScN thin films lead to its tunable carrier concentration from 5×10^{18} to $1.6 \times 10^{21} \text{ cm}^{-3}$ range, while retaining a moderately high mobility that gives rise to tunable high-quality low-loss SWIR plasmon- and LWIR high-quality phonon-polariton resonance that was considered to be mutually exclusive previously.

ScN is a rocksalt group-III (B) semiconducting transition-metal-nitride (TMN) and exhibits corrosion-resistant high hardness, high melting temperature ($\sim 2600^\circ\text{C}$) and is stable at ambient temperature and pressure³⁰⁻³⁴. Due to the degenerate semiconducting nature with a direct bandgap of 2.2 eV and indirect gap of 0.9 eV^{35,36}, ScN has attracted significant interest in recent years for thermoelectric energy conversion³⁷. Lattice-matched (111) ScN seed-layers are also utilized to reduce the dislocation densities in (0002) GaN epilayers for light-emitting diodes^{38,39}. As-deposited ScN thin films exhibit an *n*-type carrier concentration of $(2-4) \times 10^{20} \text{ cm}^{-3}$ primarily due to the presence of oxygen impurities and exhibit a mobility in the 60-90 cm^2/Vs range. Due to such high carrier concentrations, Fermi level in ScN resides inside the conduction band, about 0.2-0.3 eV inside the conduction band minima³⁵. Recently, Mg-hole doping is used to reduce the high carrier concentration and *p*-type ScN is achieved with high mobility ($\sim 25 \text{ cm}^2/\text{Vs}$)⁴⁰. Photoemission measurement and first-principles calculation have demonstrated that both the oxygen and magnesium-doping in ScN do not introduce defect states within its bandgap, and they do not alter the valence and conduction band edges⁴¹. Due to such a rigid electronic band, the Fermi level moves freely from the conduction band to the valence band, giving rise to very high electron and hole-concentrations and large thermoelectric power factors³⁷. Moreover, since optical phonons in ScN exhibit a maximum energy of $\sim 84 \text{ meV}$ ⁴², plasmon-resonances in the SWIR region are well-separated from the phonon-polariton resonance. Therefore, high-mobility and tunable carrier concentration in ScN provide a perfect testbed to achieve high-quality plasmon- and phonon-polariton in one host medium.

ScN thin films with carrier concentration ranging from $1.6 \times 10^{21} \text{ cm}^{-3}$ to $5 \times 10^{18} \text{ cm}^{-3}$ (see Table 1) are deposited inside an ultra-high vacuum (UHV) chamber at a base pressure of $(2-4) \times 10^{-9}$ Torr (see Methods). Without any intentional doping, *n*-type ScN films exhibit a carrier concentration of $3.6 \times 10^{20} \text{ cm}^{-3}$ with a mobility of 43 cm^2/Vs . Intentional oxygen-doping increase its carrier concentration up to $1.6 \times 10^{21} \text{ cm}^{-3}$, while Mg-hole doping reduces carrier concentration to as low as $5 \times 10^{18} \text{ cm}^{-3}$. Though the intentional doping reduces the mobility slightly, it remains sufficiently high (see Table 1) for achieving low-loss resonances.

Plasmon-polariton resonance

The $\{\{\epsilon\}\}_1$ of ScN (measured with a spectroscopic ellipsometer, see Fig. 1a, Methods and Supplementary) with the highest carrier concentration of $1.6 \times 10^{21} \text{ cm}^{-3}$ exhibits a positive-to-negative cross-over at $1.83 \mu\text{m}$ that is representative of the onset of its plasmonic character (see Fig. 1b). At longer wavelengths, $|\{\{\epsilon\}\}_1|$ increases monotonically due to the increasing metallic response. The optical loss, characterized by the imaginary component of the dielectric permittivity ($\{\{\epsilon\}\}_2$) at $\{\lambda\}_p$ is 1.2, which is smaller than the $\{\{\epsilon\}\}_2$ of visible wavelength plasmonic materials such as Au⁴³, TiN⁴⁴ etc. at their respective $\{\lambda\}_p$. $\{\{\epsilon\}\}_2$ of ScN is also comparable with the NIR plasmonic materials such as ITO, AZO; as well as with the MIR plasmonic materials such as CdO (see Supplementary Fig. S1 and S2). Below $1.83 \mu\text{m}$, ScN acts as a dielectric medium with positive $\{\{\epsilon\}\}_1$ and a peak in $\{\{\epsilon\}\}_2$ near $\sim 430 \text{ nm}$ (see Supplementary Fig. S3) corresponds to the direct bandgap interband transition. Polarization-dependent reflectivity measurements (see Fig. 1b) show a clear dip near $\{\lambda\}_p$ representative of the plasmonic nature. Angle-dependent reflectivity measurements (see Fig. 1c) clearly show the Brewster's angle in the p -polarized/ s -polarized reflection curve. The calculated reflectance spectrum (see Fig. 1d) utilizing the permittivity of ScN in the Fresnel's equation (see Supplementary section 5) matches well with the measured reflectivity which highlights consistency between the experiment and ellipsometry data fitting.

Excitation of the surface plasmon-polaritons (SPP) is demonstrated (see Fig. 1e) with polarization-dependent reflectivity measurement in the attenuated-total-reflection (ATR) configuration inside an FTIR-spectrometer in the Kretschmann configuration at 45° angle-of-incidence. Diamond is used as a high refractive index medium and to provide the additional momentum for the light coupling to the SPP modes. A clear dip in the p -/ s -polarized reflection spectrum at $\sim 1.95 \mu\text{m}$ (see Fig. 1f) with a full-width-at-the-half-maxima (FWHM) of $\sim 0.27 \mu\text{m}$ demonstrate the coupling of energy from the incident radiation to the SPP mode. The SPP dispersion⁴⁵ is calculated (see Fig. 1f) taking into account the measured dielectric permittivity of ScN that show close matching of the $\{\lambda\}_{\text{SPP}}$ (wavelength corresponding to the SPP mode frequency) with the experimentally measured dip in reflectivity curve.

While the above analysis unambiguously demonstrates SWIR plasmon excitation in ScN, spectral position of the plasmon-resonance and the SPP mode frequencies are varied by altering the carrier concentration (see Eq. 2) through doping control. With a decrease in the carrier concentration from $1.6 \times 10^{21} \text{ cm}^{-3}$ (a) to $1.4 \times 10^{21} \text{ cm}^{-3}$ (b), $7.7 \times 10^{20} \text{ cm}^{-3}$ (c) and $3.3 \times 10^{20} \text{ cm}^{-3}$ (d), ellipsometry measurements show that the $\{\lambda\}_p$ shifts from $1.83 \mu\text{m}$ to $2.08 \mu\text{m}$, $2.25 \mu\text{m}$ and $2.35 \mu\text{m}$, respectively (see Fig. 2a). Such monotonic red-shift in the $\{\lambda\}_p$ is consistent with the predictions from the Drude model (see Eq. 3) of dielectric permittivity, and cover a wide SWIR range. $\{\{\epsilon\}\}_2$ of ScN with $3.3 \times 10^{20} \text{ cm}^{-3}$ carrier densities show the lowest value, primarily due to its higher mobility of $43 \text{ cm}^2/\text{Vs}$. Since the highest mobility and the lowest optical loss is obtained in the as-deposited ScN without any intentional doping, $\{\lambda\}_p$ of $2.35 \mu\text{m}$ with the lowest optical loss of 1.0 could be regarded as the baseline plasmon response in ScN. Dielectric permittivity at the longer wavelength regions ($1.5\text{-}5 \mu\text{m}$) is measured further with an IR-ellipsometer (see Supplementary Fig. S1) which demonstrates ScN's metallic response in the SWIR-to-mid-IR spectral region. Similar to the tunable

bulk plasmon frequency, tunability of the SPP mode frequencies are further demonstrated by the polarization-dependent ATR measurements, which show a dip at 2.70 μm with a FWHM of 0.56 μm for ScN with $3.3 \times 10^{20} \text{ cm}^{-3}$ (d) carrier concentrations.

The plasmonic response is further characterized by temperature-dependent Hall measurements (see Fig. 2d). The resistivity of all ScN films increases slightly with an increase in temperature (see Fig. 2e) which is representative of their degenerate semiconducting or semi-metallic nature due to high carrier concentrations. On the other hand, mobility decreases with an increase in temperature as found in Fig. 2f. A combination of ionized impurity and dislocation scattering model is found to fit the temperature-dependence of mobility very well with a high dislocation density in the 10^9 - 10^{11} cm^{-2} range (see Supplementary Fig. S4), which can be seen as well in transmission electron microscopy (TEM) images. The carrier concentration of the ScN films remain nearly unchanged within the measured temperature range (see Fig. 2g).

Temperature-dependent dielectric permittivity is measured further to highlight the refractory plasmonic behavior of ScN. Results show that with an increase in temperature from 100 K-to-500 K, λ_p exhibits a redshift from 1.76 μm to 1.83 μm (see Fig. 3a), and ϵ_2 increases from 0.95 to 1.32 at the corresponding λ_p for the ScN film with $1.6 \times 10^{21} \text{ cm}^{-3}$ carrier concentrations. Such an increase in λ_p and optical losses, especially at longer wavelengths (see Fig. 3b) can be directly attributed to the decrease in mobility as shown in Fig. 3c. However, near the λ_p wavelength region, the increase in ϵ_2 is rather small that highlight the suitability of ScN for high-temperature applications. It is important to note here that though the permittivity is measured till 500 K due to instrumental limitations, ScN exhibits a high melting temperature of $\sim 2600^\circ\text{C}$, and hence could be useful for many plasmonic applications at high-temperatures.

With the above refractory plasmonic properties in the SWIR spectral range, ScN's suitability for various nano-photonic applications^{18,46} such as in SPP waveguides, localized surface-plasmon-resonance (LSPR), epsilon-near-zero (ENZ), hyperbolic metamaterials (HMM), and transformation optics are determined. Each of these applications requires its own optimum operating conditions that are determined by the structure and geometry of devices, as well as material properties. Our analysis show (see Supplementary Fig. S5) that the plasmon-resonance and SPP in ScN should be useful for the non-resonant SWIR applications such as waveguides, ENZ, HMM¹⁸. As an example, ScN exhibits a high SPP propagation length (L) and low electric-field confinement length (D) that is comparable to other doped-semiconductors and CMOs for high-performance waveguides. A ratio between the L and D, referred as the figure-of-merit (M_1^{2D})⁴⁷ is high in ScN and compares well to its alternatives in the near and mid-IR spectral range. Similarly, a low ϵ_2 of 1.00 at λ_p should be suitable for ENZ device applications⁴⁸ such as photon funnels, or spatial filtering for beaming. Even for the localized SPP resonance, the figure-of-merit (FOM) of ScN is comparable to its counterparts. Nevertheless, it should be highlighted that with more advanced deposition methods such as molecular-beam-epitaxy (MBE) and

hybrid vapor phase epitaxy, mobility of ScN could be increased further which should improve its performance metrics.

Phonon-polariton resonance

While the carrier concentration control leads to the SWIR plasmonic response in ScN, demonstration of SPh.P. excitation requires that the electronic resonance do not contribute to the total dielectric permittivity in the LWIR spectral range. To achieve this condition, Mg (hole)-doped ScN films with low carrier concentrations are deposited (see Table 1). To separate the contributions of MgO (substrate) phonon modes, a 100 nm IR reflective TiN buffer layer is deposited on (001) MgO substrates before ScN depositions (see Supplementary Fig. S6). Infrared reflectivity measurement (see Fig. 4a) of ScN with $5 \times 10^{18} \text{ cm}^{-3}$ carrier concentration shows well-defined Reststrahlen band (see Fig. 4b), a highly reflective region between the TO (359 cm^{-1}) and LO (686 cm^{-1}) phonon modes where light couples with the polar optical lattice vibrations. Calculated $\{\{\epsilon\}\}_1$ is found to exhibit negative values within the Reststrahlen band, with an epsilon-near-pole (ENP) resonance at 359 cm^{-1} since light couples directly to the TO phonon mode (see Fig. 4c). Concomitantly, $\{\{\epsilon\}\}_2$ exhibits a sharp peak at the TO phonon frequency. Both LO and TO phonon frequencies are consistent with recent inelastic X-ray scattering phonon dispersion of ScN⁴².

Further, polarization-dependent ATR measurements are performed which show a dip at 626 cm^{-1} in the p -polarized light, representing coupling of light with the SPh.P mode. Calculated SPh.P dispersion is consistent with the experimental observations, and also highlight the bulk phonon-polaritons at frequencies above and below the Reststrahlen band. Performance FOM of SPh.P modes²⁶ is calculated and compared with other well-established polar dielectric materials such as SiC²⁷, h-BN²⁸, c-BN⁴⁹, AlN²⁹, and GaN⁵⁰. SPh.P FOM of ScN is found to be around two times higher than its peers due to its high $\{\{\epsilon\}\}_{\infty}$ of 12.8 (see Supplementary Fig. S7).

Microstructure characterization

While the compelling optical properties of ScN makes it an attractive IR polaritonic material, SPP waveguides, HMM, ENZ and other device implementations require low surface roughness, a lattice-matched interfaces with the substrate and compatibility with industrially relevant materials.

Scanning transmission electron microscopy (STEM), energy-dispersive x-ray spectroscopy (EDS) mapping and electron diffraction were applied to characterize the microstructure of the film. Both oxygen and magnesium-doped ScN films deposited in this work on (001) MgO substrates at high-temperatures grow epitaxially with 001 ScN || 001 MgO (see Fig. 5a and 5b). The ScN/MgO interface is sharp despite the presence of a few misfit-dislocations, resulting from the 7% lattice-mismatch between ScN and MgO. Importantly, both oxygen and magnesium dopants make homogeneous solid-solutions with ScN without any precipitations or secondary phase formations (see EDS maps in Fig. 5 c-f) resulting in a small rms. surface roughness of $\sim 2 \text{ nm}$ (see Supplementary Fig. S9). Electron energy loss

spectroscopy (EELS) O K-edge and Mg L-edges are consistent with the bonding of O with Sc and Mg with N respectively and splitting of the peaks highlight hybridization between different orbitals (see Supplementary Fig. S10). While the present work utilizes (001) MgO as a substrate with the same crystal structure, it must be mentioned that ScN films are regularly deposited on industrially important Al₂O₃ and Si substrates that should provide seamless chip integration. In addition, due to its perfect lattice-matching, ScN films have been deposited on (0001) GaN with very little defects³⁹ that would also lead to its integration with GaN-based light-emission and power electronic applications.

Concluding remarks

In conclusion, we present epitaxial refractory group-III scandium nitride (ScN) as a dual plasmon- and phonon-polariton material, where tunable plasmon resonance in the short-wave-infrared (SWIR) spectral range and the phonon-polariton in the long-wave-infrared (LWIR) region are obtained by carrier concentration control. Oxygen-doped ScN films with carrier concentrations between 10²⁰-10²¹ cm⁻³ exhibit high-quality and low-loss plasmon resonance in the 1.8-2.3 μm SWIR spectral region, where most plasmonic materials do not work satisfactorily. High figure-of-merit (FOM) surface phonon-polariton resonance is also achieved in the long-wavelength-infrared (LWIR) by reducing the carrier concentration with Mg-hole doping in ScN. Demonstration of plasmon- and phonon-polariton in one host material, ScN with doping-control makes it an attractive material for applications in waveguides, hyperbolic and epsilon-near-zero metamaterials, optical communication, solar-energy harvesting and infrared photonic applications.

Methods

ScN thin films were deposited on (001) MgO substrates with dc-magnetron sputtering (PVD Products Inc.) inside an ultrahigh vacuum chamber with a base pressure of (2-4) × 10⁻⁹ Torr. Substrates were cleaned with wet-chemical (acetone and methanol) methods before transferring to the load lock that operated at a pressure of 5 × 10⁻⁸ Torr. Sc (purity of 99.95%), targets had a dimension of 2 inch in diameter and 0.25 inch in thickness and was sputtered with 100 W DC-power. Deposition pressure of 10 mTorr inside an 9:2 Ar:N₂ mixture was used. The substrates temperatures were fixed at 750°C, and an average growth rate of 1.2 nm/min. was utilized (see Supplementary Methods for further details).

The optical characterizations were performed with spectroscopic ellipsometer (J. A. Woollam Co.) from 0.21 μm to 2.5 μm wavelength range in the reflection mode at three different angles (55⁰, 65⁰ and 75⁰) of incidences. The experimental (Psi $\left(\psi\right)$, $\text{D}\text{e}\text{t}\text{a}$) spectrum of ScN films were modeled with Drude & general oscillators (Gaussian and Tauc lorentz) in Complete EASE software (See Supplementary Methods for further details). Reflectivity data was recorded for the *p*- and *s*-polarized light. The temperature-dependent optical properties were measured with a cryostat from 100K-500K temperature range at 70⁰ angle of incidence. The cryostat

chamber was attached with a turbo-molecular pump leading to a chamber pressure of 10^{-7} Torr to reduce possibilities of oxidation.

Room-temperature transport data were measured with the Van der Pauw technique using an Ecopia HMS-3000 Hall measurement System. Temperature-dependent transport measurements were carried out using a Quantum Design MPMS system.

Infrared reflection and polarized attenuated-total-reflection (ATR) were performed with Bruker V70v Fourier Transform Infrared (FTIR) vacuum spectrometer using pyroelectric deuterated triglycine sulfate (DTGS) detector (for 100 cm^{-1} to 4000 cm^{-1} spectral range) and mercury cadmium telluride (MCT) detector (for 1000 cm^{-1} to 8000 cm^{-1} spectral range) with 4 cm^{-1} resolutions for 120 scans. (See Supplementary information for details of IR optical characterization).

Cross-section STEM and EDS mapping were recorded with a monochromated and image- and probe corrected FEI Themis-Z transmission electron microscope at 300 kV. EDS maps were recorded with count rates of well above 1 million per map and background correction was performed by k-factor methods and absorption correction. EELS was recorded with the same instrument utilizing a GATAN quantum GIF Dual EELS system.

TEM sample preparation was done via Focused Ion beam (FIB). A 100 nm Pt protective cap was deposited at the target location with 5 kV electron beam followed by a $1\text{ }\mu\text{m}$ Pt+C protective cap with a 12 kV Xe beam in Thermo Fisher Scientific Helios Hydra PFIB. Trenching and lift out were done with a 30 kV Xe beam at 60, 15, 4 and 1 nA. The TEM sample was welded to Mo grid using a 30 kV Xe beam Pt weld. Thinning was done with tilt angles of $\pm 1.5^\circ$ with currents of 300, 100 and 30 pA, checking for electron transparency using a 5 kV electron beam with a secondary electron detector. When the ROI was thin enough it was polished with 5 kV Xe beam with tilt angles of $\pm 3.5^\circ$. Final cleaning was performed with 2 kV Xe beam with tilt angles of $\pm 5.5^\circ$.

Declarations

Acknowledgments: KCM, and BS acknowledge International Centre for Materials Science (ICMS) and Sheikh Saqr Laboratory (SSL) in JNCASR for support. B.S. acknowledges the Science and Engineering Research Board (SERB) of the Government of India, Start-Up Research Grant No. SRG/2019/000613 for financial support. KCM thank Council of Scientific & Industrial Research (CSIR) for fellowship. M.G. and AIKP acknowledges the facilities of Sydney Microscopy and Microanalysis at The University of Sydney. SS acknowledges DST-FIST for supporting spectroscopy facility at CeNSE, IISc.

Author contributions: KCM and BS conceived this project. KCM and DR deposited the thin films. KCM performed the optical experiments and modeling. SA performed the electrical measurements, AIKP performed the TEM sample preparation and MG performed the TEM imaging and analysis. PR and SS performed the IR ellipsometer measurement, KCM and BS analyzed the results. All authors discussed and contributed to the preparation of the manuscript.

Additional information: Supplementary information is available in the online version of the paper. Reprints and permissions information is available online at .

Correspondence and requests for materials should be addressed to BS.

Competing interests: The authors declare no competing interests

References

1. Venema, L. *et al.* The quasiparticle zoo. *Nat. Phys.* **12**, 1085–1089 (2016).
2. Basov, D. N., Fogler, M. M. & García De Abajo, F. J. Polaritons in van der Waals materials. *Science* **354**, (2016).
3. Low, T. *et al.* Polaritons in layered two-dimensional materials. *Nat. Mater.* **16**, 182–194 (2017).
4. Sanvitto, D. & Kéna-Cohen, S. The road towards polaritonic devices. *Nat. Mater.* **15**, 1061–1073 (2016).
5. Schneider, C. *et al.* An electrically pumped polariton laser. *Nature* **497**, 348–352 (2013).
6. Azzam, S. I. *et al.* Ten years of spasers and plasmonic nanolasers. *Light Sci. Appl.* **9**, (2020).
7. Yang, Y. *et al.* High-harmonic generation from an epsilon-near-zero material. *Nat. Phys.* **15**, 1022–1026 (2019).
8. Caspani, L. *et al.* Enhanced Nonlinear Refractive Index in ϵ -Near-Zero Materials. *Phys. Rev. Lett.* **116**, 233901 (2016).
9. Reshef, O., De Leon, I., Alam, M. Z. & Boyd, R. W. Nonlinear optical effects in epsilon-near-zero media. *Nat. Rev. Mater.* **4**, 535–551 (2019).
10. Schuller, J. A., Taubner, T. & Brongersma, M. L. Optical antenna thermal emitters. *Nat. Photonics* **3**, 658–661 (2009).
11. Starko-Bowes, R. *et al.* High-Temperature Polaritons in Ceramic Nanotube Antennas. *Nano Lett.* **19**, 8565–8571 (2019).
12. Wang, T. *et al.* Phonon-Polaritonic Bowtie Nanoantennas: Controlling Infrared Thermal Radiation at the Nanoscale. *ACS Photonics* **4**, 1753–1760 (2017).
13. Caldwell, J. D. *et al.* Low-loss, extreme subdiffraction photon confinement via silicon carbide localized surface phonon polariton resonators. *Nano Lett.* **13**, 3690–3697 (2013).
14. Jahani, S. & Jacob, Z. All-dielectric metamaterials. *Nat. Nanotechnol.* **11**, 23–36 (2016).
15. Caldwell, J. D. *et al.* Atomic-scale photonic hybrids for mid-infrared and terahertz nanophotonics. *Nat. Nanotechnol.* **11**, 9–15 (2016).
16. Law, S., Yu, L. & Wasserman, D. Epitaxial growth of engineered metals for mid-infrared plasmonics. *J. Vac. Sci. Technol. B, Nanotechnol. Microelectron. Mater. Process. Meas. Phenom.* **31**, 03C121 (2013).
17. Ginn, J. C., Jarecki, R. L., Shaner, E. A. & Davids, P. S. Infrared plasmons on heavily-doped silicon. *J. Appl. Phys.* **110**, 043110 (2011).

18. Naik, G. V., Shalaev, V. M. & Boltasseva, A. Alternative plasmonic materials: Beyond gold and silver. *Adv. Mater.* **25**, 3264–3294 (2013).
19. Runnerstrom, E. L., Kelley, K. P., Sachet, E., Shelton, C. T. & Maria, J. P. Epsilon-near-Zero Modes and Surface Plasmon Resonance in Fluorine-Doped Cadmium Oxide Thin Films. *ACS Photonics* **4**, 1885–1892 (2017).
20. Sachet, E. *et al.* Dysprosium-doped cadmium oxide as a gateway material for mid-infrared plasmonics. *Nat. Mater.* **14**, 414–420 (2015).
21. Yan, H. *et al.* Damping pathways of mid-infrared plasmons in graphene nanostructures. *Nat. Photonics* **7**, 394–399 (2013).
22. Brar, V. W., Jang, M. S., Sherrott, M., Lopez, J. J. & Atwater, H. A. Highly confined tunable mid-infrared plasmonics in graphene nanoresonators. *Nano Lett.* **13**, 2541–2547 (2013).
23. Taliercio, T. & Biagioni, P. Semiconductor infrared plasmonics. *Nanophotonics* **8**, 949–990 (2019).
24. Folland, T. G., Nordin, L., Wasserman, D. & Caldwell, J. D. Probing polaritons in the mid- to far-infrared. *J. Appl. Phys.* **125**, 191102 (2019).
25. Stroschio, M. A. & Dutta, M. *Phonons in Nanostructures*. (Cambridge University Press, 2001). doi:10.1017/CBO9780511534898.
26. Caldwell, J. D. *et al.* Low-loss, infrared and terahertz nanophotonics using surface phonon polaritons. *Nanophotonics* **4**, 44–68 (2015).
27. Hillenbrand, R., Taubner, T. & Keilmann, F. Phonon-enhanced light-matter interaction at the nanometre scale. *Nature* **418**, 159–162 (2002).
28. Caldwell, J. D. *et al.* Sub-diffractive volume-confined polaritons in the natural hyperbolic material hexagonal boron nitride. *Nat. Commun.* **5**, 5221 (2014).
29. Ng, S. S., Hassan, Z. & Abu Hassan, H. Experimental and theoretical studies of surface phonon polariton of AlN thin film. *Appl. Phys. Lett.* **90**, 2005–2008 (2007).
30. Biswas, B. & Saha, B. Development of semiconducting ScN. *Phys. Rev. Mater.* **3**, 020301 (2019).
31. Eklund, P., Kerdsonpanya, S. & Alling, B. Transition-metal-nitride-based thin films as novel energy harvesting materials. *J. Mater. Chem. C* **4**, 3905–3914 (2016).
32. Gall, D. *et al.* Electronic structure of ScN determined using optical spectroscopy, photoemission, and ab initio calculations. *Phys. Rev. B - Condens. Matter Mater. Phys.* **63**, 1251191–1251199 (2001).
33. Gall, D. *et al.* Growth of poly- and single-crystal ScN on MgO(001): Role of low-energy N₂ irradiation in determining texture, microstructure evolution, and mechanical properties. *J. Appl. Phys.* **84**, 6034–6041 (1998).
34. Maurya, K. C., Biswas, B., Garbrecht, M. & Saha, B. Wave-Vector-Dependent Raman Scattering from Coupled Plasmon–Longitudinal Optical Phonon Modes and Fano Resonance in n-type Scandium Nitride. *Phys. Status Solidi - Rapid Res. Lett.* **13**, 1–6 (2019).
35. Stampfl, C., Mannstadt, W., Asahi, R. & Freeman, A. J. Electronic structure and physical properties of early transition metal mononitrides: Density-functional theory LDA, GGA, and screened-exchange

- LDA FLAPW calculations. *Phys. Rev. B - Condens. Matter Mater. Phys.* **63**, 1–11 (2001).
36. Mu, S., Rowberg, A. J. E., Leveillee, J., Giustino, F. & Van de Walle, C. G. First-principles study of electron transport in ScN. *Phys. Rev. B* **104**, 075118 (2021).
37. Rao, D. *et al.* High mobility and high thermoelectric power factor in epitaxial ScN thin films deposited with plasma-assisted molecular beam epitaxy. *Appl. Phys. Lett.* **116**, 152103 (2020).
38. Moram, M. A., Zhang, Y., Kappers, M. J., Barber, Z. H. & Humphreys, C. J. Dislocation reduction in gallium nitride films using scandium nitride interlayers. *Appl. Phys. Lett.* **91**, 152101 (2007).
39. Acharya, S. *et al.* Twinned growth of ScN thin films on lattice-matched GaN substrates. *Mater. Res. Bull.* **143**, 111443 (2021).
40. Saha, B. *et al.* Compensation of native donor doping in ScN: Carrier concentration control and p-type ScN. *Appl. Phys. Lett.* **110**, 252104 (2017).
41. Nayak, S. *et al.* Rigid-band electronic structure of scandium nitride across the n -type to p -type carrier transition regime. *Phys. Rev. B* **99**, 161117 (2019).
42. Uchiyama, H. *et al.* Phonon Lifetime Observation in Epitaxial ScN Film with Inelastic X-Ray Scattering Spectroscopy. *Phys. Rev. Lett.* **120**, 235901 (2018).
43. P. B. Johnson and R. W. Christy. Optical Constant of the Nobel Metals. *Phys. Rev. B* **6**, 4370–4379 (1972).
44. Maurya, K. C., Shalaev, V. M., Boltasseva, A. & Saha, B. Reduced optical losses in refractory plasmonic titanium nitride thin films deposited with molecular beam epitaxy. *Opt. Mater. Express* **10**, 2679 (2020).
45. Maier, S. A. *Plasmonics: Fundamentals and Applications*. Springer (2007).
doi:10.1016/j.aca.2010.06.020.
46. Wang, Z., Chen, C., Wu, K., Chong, H. & Ye, H. Transparent Conductive Oxides and Their Applications in Near Infrared Plasmonics. *Phys. Status Solidi Appl. Mater. Sci.* **216**, 1–12 (2019).
47. Berini, P. Figures of merit for surface plasmon waveguides. *Opt. Express* **14**, 13030–13042 (2006).
48. Kinsey, N., DeVault, C., Boltasseva, A. & Shalaev, V. M. Near-zero-index materials for photonics. *Nat. Rev. Mater.* **4**, 742–760 (2019).
49. Gielisse, P. J. *et al.* Lattice Infrared Spectra of Boron Nitride and Boron Monophosphide. *Phys. Rev.* **155**, 1039–1046 (1967).
50. Torii, K. *et al.* An attenuated-total-reflection study on the surface phonon-polariton in GaN. *J. Phys. Condens. Matter* **12**, 7041–7044 (2000).

Table 1

Table 1

Carrier concentration, mobility, and resistivity of ScN thin films are presented. The wavelength ($\lambda\rho$) corresponding to the plasmon- and phonon-polariton resonance frequency are listed.

ScN films	Carrier concentration (cm^{-3})	Mobility ($\text{cm}^2\text{V}^{-1}\text{s}^{-1}$)	Resistivity ($\Omega\text{-cm}$)	Cross-over Wavelength $\lambda\rho$ (μm)
SWIR Plasmon-polariton Resonance				
ScN (a)	1.6×10^{21}	29	1.4×10^{-4}	1.83
ScN (b)	1.4×10^{21}	6	7.6×10^{-4}	2.08
ScN (c)	7.7×10^{20}	22	3.8×10^{-4}	2.25
ScN (d)	3.3×10^{20}	43	4.4×10^{-4}	2.35
LWIR Phonon-polariton Resonance				
ScN (e)	4.3×10^{19}	12.6	1.0×10^{-2}	14.58 (LO) 27.80 (TO)
ScN (f)	5.0×10^{18}	9.7	1.3×10^{-1}	14.58 (LO) 27.80 (TO)

Figures

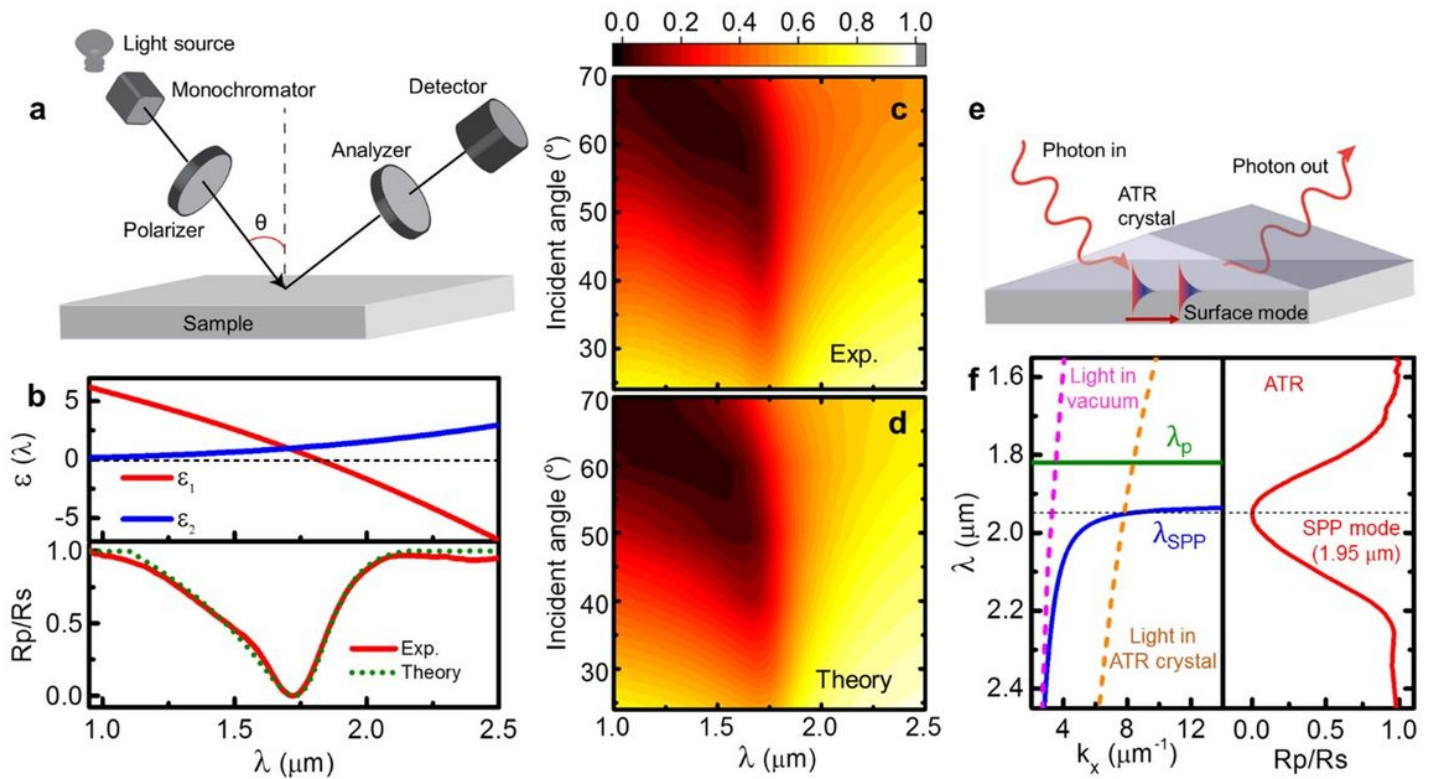


Figure 1

Plasmon-polariton in ScN. **a**, Schematic diagram of a spectroscopic ellipsometer. **b**, The real (ϵ_1) and imaginary (ϵ_2) component of the dielectric permittivity of ScN film with the highest carrier concentration of $1.6 \times 10^{21} \text{ cm}^{-3}$ is presented. ScN becomes plasmonic after $1.83 \mu\text{m}$. ($\epsilon_1 < 0$) with the optical loss of 1.2 at the wavelength (λ_p) corresponding to its plasma frequency. Experimentally measured normalized reflectivity of ScN film is plotted as the ratio between the p -polarized to s -polarized light intensity which shows a dip near the λ_p . **c**, Angle-dependent reflectivity curve of ScN film is presented. Brewster's angle is visible in the reflectivity curve. **d**, Fresnel's equation-based theoretically calculated reflection curve matches well with the experimentally measured reflection curve. **e**, A schematic diagram of the ATR configuration for surface mode excitation. **f**, Theoretically calculated SPP dispersion (blue) along with the ATR-measured reflection curve that shows SPP mode excitation at $1.95 \mu\text{m}$. The light lines in the vacuum and in ATR crystal are shown by the magenta and orange dotted curves respectively. The bulk plasma wavelength (λ_p) is shown with the green line.

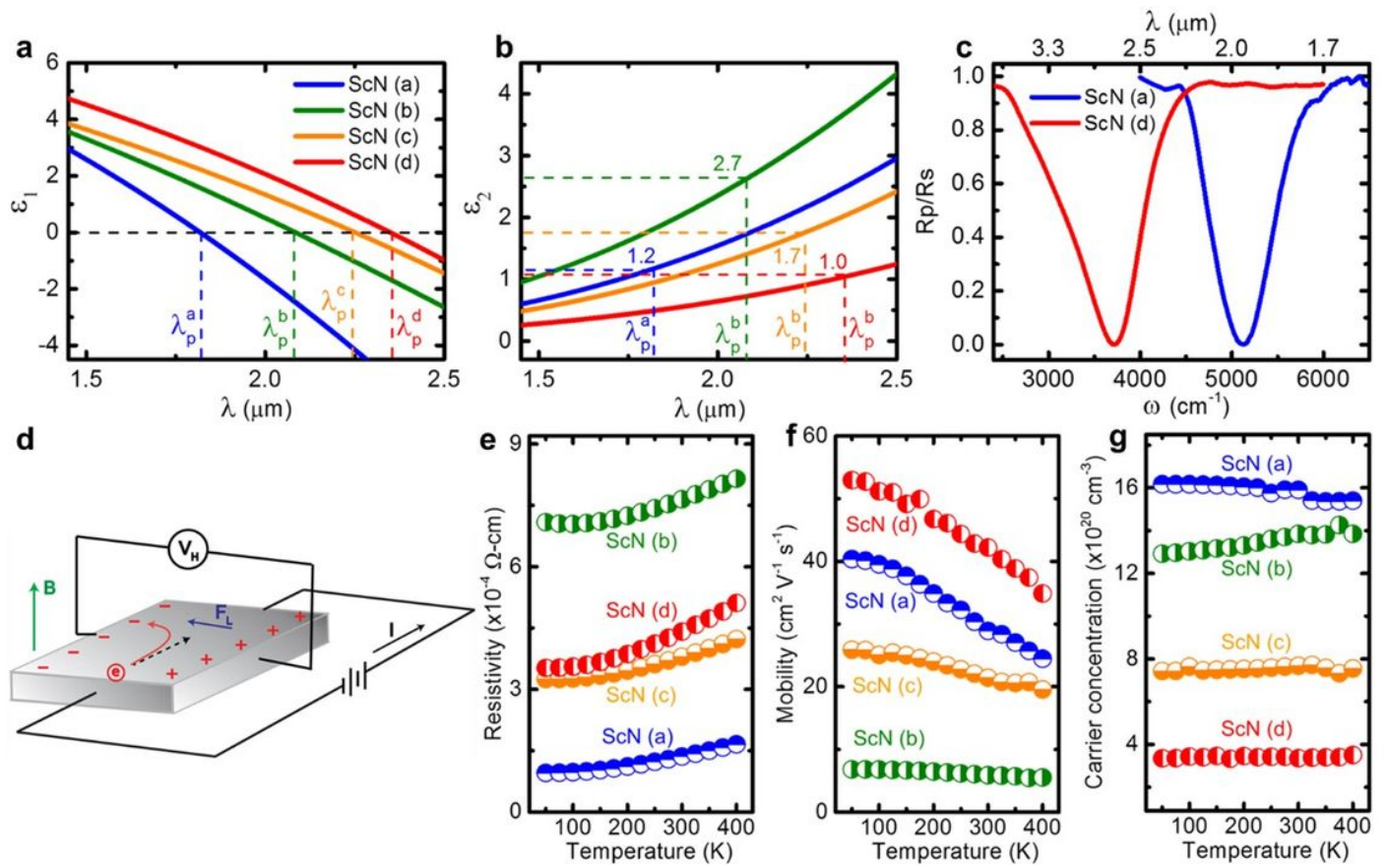


Figure 2

Tunable SWIR plasmon response and electrical properties of ScN. **a**, ϵ_1 and **b**, ϵ_2 of ScN films with varying carrier concentrations are presented. With the decrease in carrier concentration, λ_p shifts to longer wavelengths. λ_p of 2.35 μm and corresponding ϵ_2 of 1.0 is obtained for as-deposited ScN film without any intentional doping which makes it a high-quality and low-loss SWIR plasmonic material. **c**, Normalized reflectivity curves of ScN with $1.6 \times 10^{21} \text{ cm}^{-3}$ (a) and $3.3 \times 10^{20} \text{ cm}^{-3}$ (d) are presented as the ratio between p -polarized and s -polarized intensity (R_p/R_s) obtained from the ATR measurements **d**, Schematic diagram of the Hall measurement is shown. Temperature-dependent **e**, resistivity; **f**, mobility and **g**, carrier concentration of ScN films are shown which highlights its degenerate semiconducting nature.

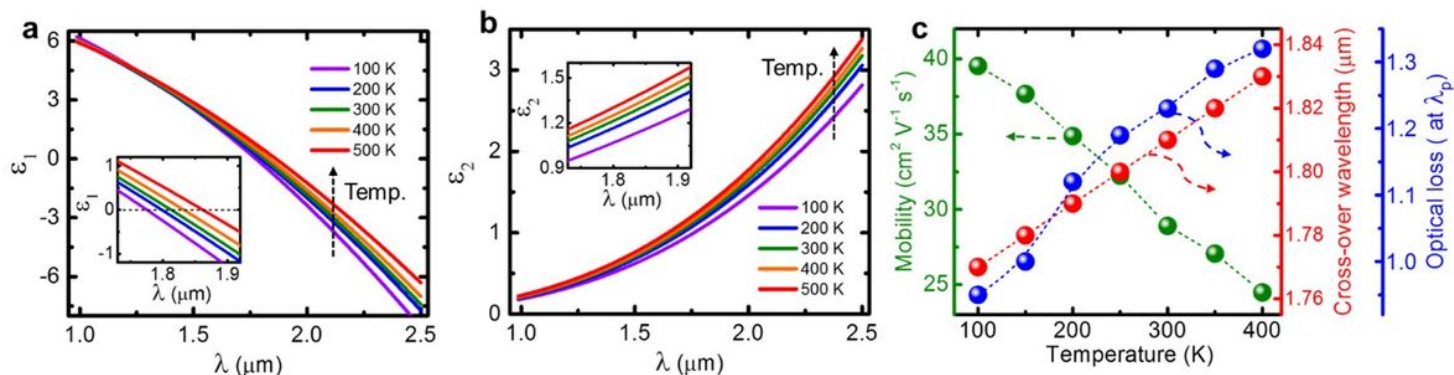


Figure 3

Temperature-dependent dielectric constants of ScN. Temperature-dependent **a**, ϵ_1 **b**, ϵ_2 of the ScN thin film with $1.6 \times 10^{21} \text{ cm}^{-3}$ carrier concentrations are presented. With an increased temperature, λ_p and the optical loss increase. **c**, Cross-over wavelength (λ_p) and optical loss was found to increase with increasing temperature as mobility is decreasing.

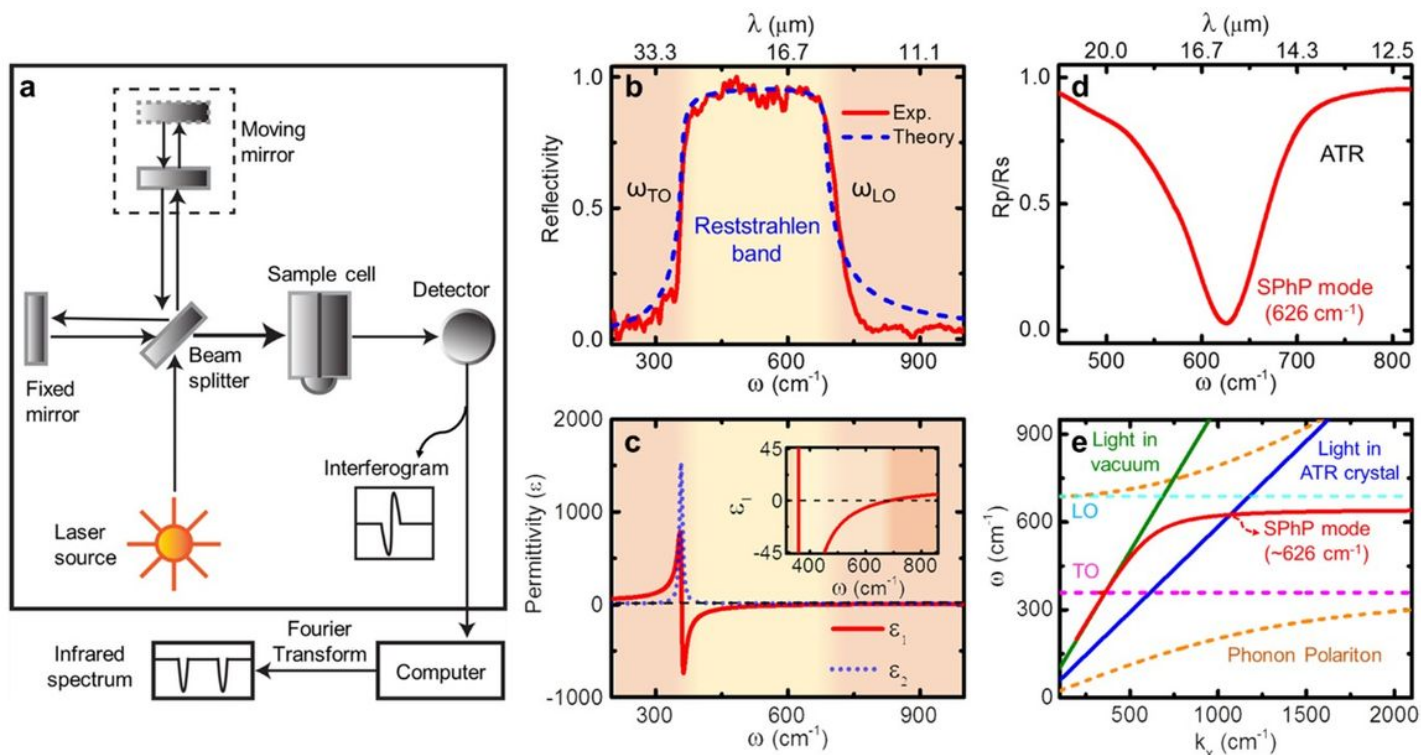


Figure 4

Phonon-polariton in ScN. **a**, Schematic diagram of Fourier-transform infrared spectrometer (FTIR). **b**, Normalized FTIR reflection (red) spectra of ScN film is shown and the calculated reflection spectrum is presented (in blue shade). **c**, Calculated dielectric permittivity (ϵ) of ScN thin film showing negative ϵ_1 within the Reststrahlen band. **d**, Normalized reflection spectra obtained from the ATR measurement

showing excitation of the SPh.P mode with p -polarized light. **e**, Theoretically calculated dispersion of SPh.P is presented. The light lines, in the vacuum and ATR crystal, are shown by the green and blue curve respectively. The frequency positions of ω_{L0} and ω_{T0} are shown by cyan and magenta dotted lines respectively. Lower and upper bulk phonon polaritons are shown by the orange dotted curve.

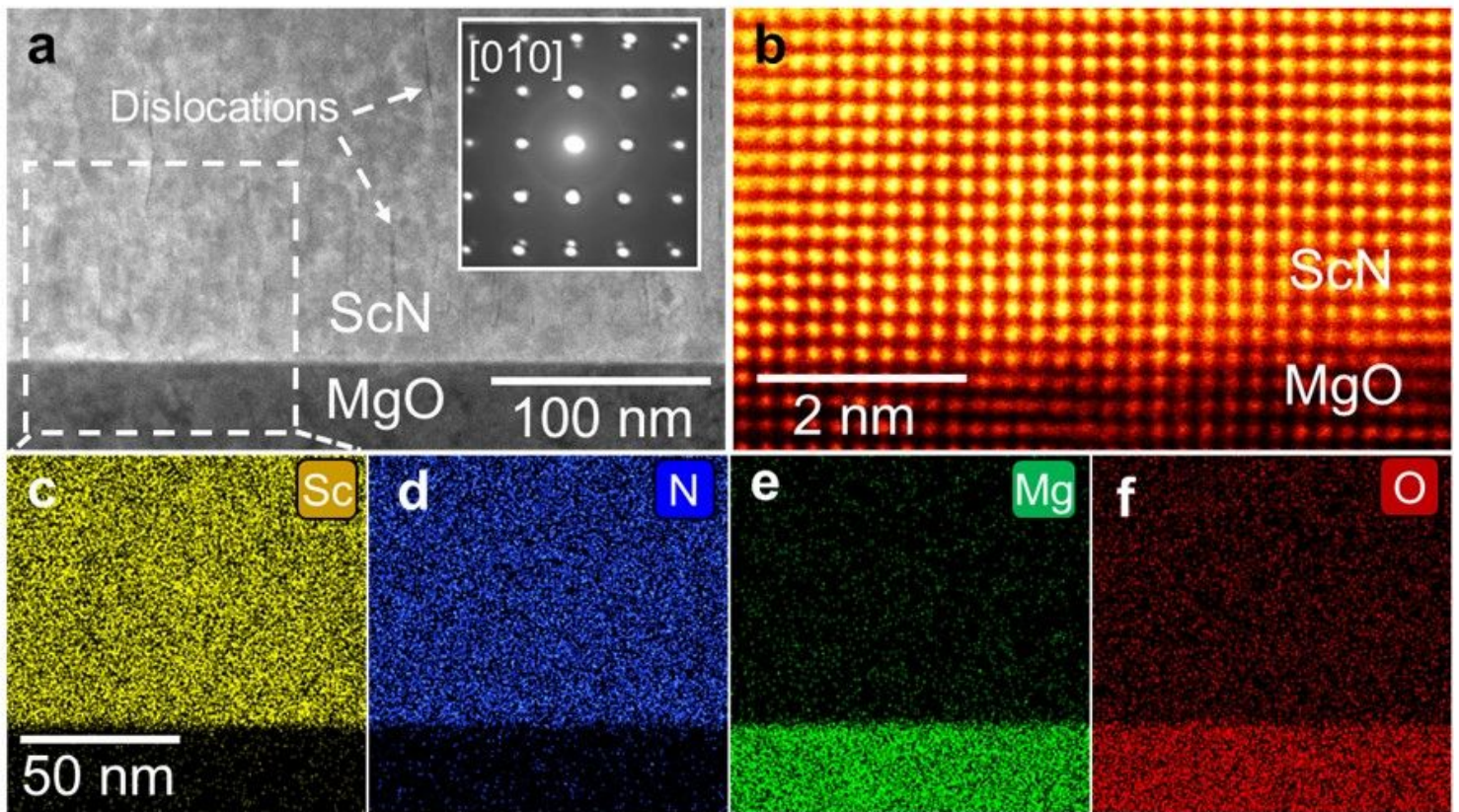


Figure 5

STEM images and EDS maps of ScN deposited on (001) MgO substrate. **a**, Low-magnification STEM image showing homogeneous and uniform ScN growth with a few dislocations. The electron diffraction pattern in the inset confirms the cubic epitaxial growth. **b**, Atomic resolution STEM image of the ScN/MgO demonstrating a sharp interface. STEM-EDS elemental mapping of **c**, Sc; **d**, N; **e**, Mg; **f**, O shows the homogeneous elemental distribution.

Supplementary Files

This is a list of supplementary files associated with this preprint. Click to download.

- [ScNPolaritonSupportingInfo.docx](#)